JOURNAL OF GUIDANCE, CONTROL, AND DYNAMICS
Vol. 33, No. 6, November–December 2010

Method to Design Ballistic Capture in the Elliptic Restricted Three-Body Problem

Nicola Hyeraci* and Francesco Topputo†
Politecnico di Milano, Milano, 20156, Italy

DOI: 10.2514/1.49263

This paper presents a systematic method to design ballistic capture orbits upon planet arrival in interplanetary transfers. The capture orbit is defined in the elliptic restricted three-body problem. This allows the application of the presented method to such cases where the circular problem fails in describing the three-body dynamics. The method is formulated using the concept of stable sets computed through an algorithmic definition. Stable sets are manipulated to generate the capture subset containing candidate ballistic capture orbits that perform a prescribed number of revolutions about the smaller primary. The method is used to design capture orbits near Mars and Mercury.

Nomenclature

a	=	semimajor axis of osculating orbit of P_3
a_p	=	semimajor axis of $P_1 - P_2$ system
C	=	Jacobi energy
$\mathcal{C}$	=	capture subset
e	=	eccentricity of osculating orbit of P_3
e_p	=	eccentricity of $P_1 - P_2$ system
f	=	true anomaly of P_2
H_2	=	Kepler energy of P_3 relative to P_2
h	=	periapsis altitude
J_C	=	Jacobi integral, circular problem
J_E	=	Jacobi integral, elliptic problem
m_1	=	mass of P_1
m_2	=	mass of P_2
N	=	number of initial conditions
P_1	=	larger primary
P_2	=	smaller primary
P_3	=	third body
R_{12}	=	$P_1 - P_2$ distance
R_{eq}	=	equatorial radius of P_2
r_1	=	distance of P_3 from P_1
r_2	=	distance of P_3 from P_2
r_{LC}	=	radius of regularizing disc
t	=	time
u, v	=	regularized coordinates of P_3
v_2	=	speed of P_3 relative to P_2
$\boldsymbol{w}$	=	regularized vector, $\boldsymbol{w} = u + iv$
$\mathcal{W}$	=	stable set
$\boldsymbol{x}$	=	state of P_3, $\boldsymbol{x} = (x, y, x', y')$
x, y	=	coordinates of P_3
θ_i	=	angle between x-axis and P_iP_3 line, $i = 1, 2$
μ	=	mass parameter
τ	=	independent variable of regularized equations
ω	=	potential of the elliptic problem
Ω	=	potential of the circular problem

Superscripts

$()'$	=	differentiation with respect to true anomaly
$\dot{()}$	=	differentiation with respect to time

Subscript

$()_{x,y}$	=	partial derivative with respect to x, y

I. Introduction

THE study of ballistic capture orbits for space applications dates back to the rescue of the Japanese spacecraft Hiten in 1991 [1]. In essence, a ballistic capture orbit reduces the relative hyperbolic excess velocity upon arrival, typical of a patched-conics approach. This is achieved by better exploiting the gravitational nature of the solar system instead of using the classic Keplerian decomposition. The reduced speed at arrival yields lower energy levels than those associated to hyperbolic approaches; for this reason these transfers are labeled *low energy transfers*. This, in turn, allows saving the propellant mass needed to stabilize the spacecraft about the arrival body.

Hiten performed a ballistic capture at the moon [2], so demonstrating the feasibility of these orbits for practical applications. In a typical Earth–Moon low energy transfer, a portion of trajectory is defined in regions where the gravitational attractions of the sun, the Earth, and the moon tend to balance. The moon is then approached from the far side. This is called *external* low energy transfer. NASA's forthcoming GRAIL mission will exploit this concept to reach the moon.‡ A ballistic capture at the moon was also achieved by SMART-1 [3]: the capture mechanism in this case exploits the balancing of the gravitational attractions of the Earth and the moon; this is an *internal* low energy transfer. In the frame of interplanetary transfers, a ballistic capture at Mercury is being designed for ESA's BepiColombo mission [4]; here, beside the mere propellant mass saving, a ballistic capture has been chosen to circumvent possible single-point failures of a classical chemical orbit insertion burn. The dynamics of the sun–Mercury gravitational field is used.

The ballistic capture is a chaotic process defined under nonintegrable dynamics. Therefore, the design of ballistic capture orbits is nontrivial, and lacks a systematic way to derive arrival orbits matching mission constraints. The design of ballistic capture trajectories can be performed by following two methods, which are based on two different philosophies. The first one analyzes the structure of the phase space about the collinear equilibrium points of the circular restricted three-body problem. It can be shown that the invariant manifolds of the periodic orbits around the collinear points act as separatrix for the states of motion [5]. Orbits inside these invariant manifold tubes can transit from one region of the space to another, and they can be achieved by globally extending invariant manifolds together with the use of suitable Poincaré sections [6]. This approach

Received 8 February 2010; revision received 3 August 2010; accepted for publication 5 August 2010.

*Graduate Student, Aerospace Engineering Department, Via La Masa, 34.
†Postdoctoral Fellow, Aerospace Engineering Department, Via La Masa, 34.

‡Data available online at http://moon.mit.edu [retrieved January 2010].

has been successfully used to recompute Hiten's trajectory from a different perspective [7]. The same concept has also been proposed to design ballistic capture orbits upon inner planets [8]. Although the invariant manifolds technique brings out insights into the dynamics ruling the ballistic capture mechanism, it exhibits two basic drawbacks.

1) There is no apparent control on the two-body orbital elements of the final capture orbit. In the likely practical case where a final orbit with prescribed parameters is desired, no straightforward process allows us to locate appropriate regions within the invariant manifold tube; i.e., it is not possible to prune out at once regions leading to undesired capture orbits [8].

2) Equilibrium points, periodic orbits and their invariant manifolds are defined in the *circular* restricted three-body problem. They disappear when either four-body perturbations or orbital eccentricities of the primaries are taken into account. In this case, fast Lyapunov indicators [9] or Lagrangian coherent structures [10] may be used in place of invariant manifolds to understand transport phenomena. However, this is not straightforward, and requires the computation of the Lyapunov exponent vector field through a phase space sampling.

The second method exploits the concept of stable sets and weak stability boundaries; i.e., the notions behind the original design of Hiten's trajectory [2]. In principle, this method relies on a simple algorithmic definition of stability given about one of the primaries. Using this definition, stable sets and their boundaries are constructed. The latter are the weak stability boundaries [11,12]. Instead of studying the dynamics about the equilibria, this method focuses on the region about the primary, not requiring global extension of invariant manifolds. The stability definition can be easily extended to any n-body vector field. This allows using such methodology within more refined models taking into account fourth-body perturbations and planetary eccentricities [13]. In addition, stable sets can be constructed by holding fixed orbital parameters (i.e., eccentricity), so matching possible prescribed mission constraints. However, the stable sets method is not devoid of drawbacks, as the following list illustrates.

1) Stable sets are constructed by sampling the physical space and integrating thousands of orbits. In general, this process is more computationally intensive than flowing and manipulating invariant manifold sets. The number of orbits to be integrated increases with the accuracy required for the representation of the stable sets.

2) While the invariant manifolds allows us to explain free transport phenomena in the circular restricted three-body problem, the stable sets seem to have much less information from a dynamical system perspective. They are used as black-box tools to locate feasible capture orbits. Nevertheless, recent studies [11,14] show that the weak stability boundaries and the Lyapunov stable manifolds overlap for certain energy levels.

This paper elaborates on the concept of stable set to design ballistic capture orbits. In particular, stable sets are first derived and then manipulated to design orbits with prescribed orbital parameters and stability number. The latter indicates the number of turns performed about the smaller primary after capture. The dynamical model used is the planar, elliptic restricted three-body problem with the sun and an inner planet as primaries. The scope of the paper is designing ballistic capture orbits upon arrival in interplanetary transfers. Application cases concern ballistic capture at Mars and Mercury. (These two planets have nonnegligible orbital eccentricities, such that the circular problem fails at describing the restricted three-body dynamics.) The definition of backward stability is introduced and the associated stable set is suitably manipulated to automatically derive regions that support weak capture. In essence, stable sets are used to look for orbits that approach the primary in forward time (backward instability) and perform a fixed number of revolutions around it. In the case of capture at Mars, the derived solutions are connected to low-thrust interplanetary legs obtained through a shape-based approach [15]. Thus, the scope of the paper is:

1) To extend the definition of stable set and weak stability boundary in the frame of the planar, elliptic restricted three-body problem.

2) To introduce the concept of backward stability, and to derive the associated stable sets.

3) To formulate a systematic method that automatically derives ballistic capture orbits with prescribed orbital parameters and stability number.

The remainder is organized as follows. Section II describes the dynamical framework in terms of equations of motion, integrals, and regularization of dynamics. In Sec. III the stable sets are defined and shown through examples. The formulated method to derive ballistic capture orbits with prescribed stability number is illustrated in Sec. IV, which is the core of the paper. Applications to capture at Mars and Mercury are discussed in Sec. V. Final remarks are given in Sec. VI.

II. Dynamical Framework

A. Elliptic Restricted Three-Body Problem

The motion of a massless particle, P_3, is studied under the gravitational field generated by the mutual *elliptic* motion of two primaries, P_1, P_2, of masses m_1, m_2, respectively. The mass parameter of the system is $\mu = m_2/(m_1 + m_2)$. It is assumed that P_3 moves in the same plane as P_1, P_2, under the dynamics [16]

$$x'' - 2y' = \omega_x, \qquad y'' + 2x' = \omega_y \tag{1}$$

Equations of motions (1) are written in a nonuniformly rotating, barycentric, adimensional coordinate frame where P_1 and P_2 have fixed positions $(-\mu, 0)$ and $(1-\mu, 0)$, respectively, (see Fig. 1). Moreover, the coordinate frame isotropically pulsates as the $P_1 - P_2$ distance, assumed to be the unit distance, varies according to the mutual position of the two primaries on their orbits. The primes in Eq. (1) represent differentiation with respect to f, the true anomaly of the system. This is the independent variable and plays the role of the time in system (1). f is equal to zero when P_1, P_2 are at their periapse, as both primaries orbit their barycenter in similarly oriented ellipses having common eccentricity e_p. Normalizing the period of P_1, P_2 to 2π, the dependence of true anomaly on time reads [17]

$$\frac{\mathrm{d}f}{\mathrm{d}t} = \frac{(1 + e_p \cos f)^2}{(1 - e_p^2)^3} \tag{2}$$

The subscripts in Eq. (1) are the partial derivatives of

$$\omega = \frac{\Omega}{1 + e_p \cos f} \tag{3}$$

where the potential function of the circular problem, Ω, reads

$$\Omega = \frac{1}{2}(x^2 + y^2) + \frac{1-\mu}{r_1} + \frac{\mu}{r_2} + \frac{1}{2}\mu(1-\mu) \tag{4}$$

The distances in Eq. (4) are $r_1 = \sqrt{(x+\mu)^2 + y^2}$, $r_2 = \sqrt{(x+\mu-1)^2 + y^2}$. Note that setting $e_p = 0$, Eqs. (2) and (3) yield $\mathrm{d}/\mathrm{d}f = \mathrm{d}/\mathrm{d}t, \omega = \Omega$, and Eqs. (1) become those of the circular problem

$$\ddot{x} - 2\dot{y} = \Omega_x, \qquad \ddot{y} + 2\dot{x} = \Omega_y \tag{5}$$

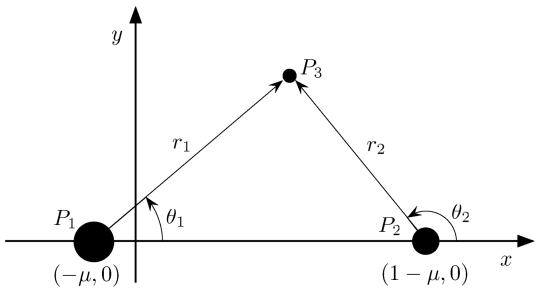

Fig. 1 Rotating, pulsating, barycentric reference system; polar coordinates.

Thus, the circular restricted three-body problem can be thought as a special case of the elliptic problem. However, unlike the circular problem, the true anomaly in Eq. (3) makes the elliptic problem nonautonomous. Thus, any qualitative feature of the elliptic problem depends on f.

B. Energetic Considerations

The anomaly-dependent integral of motion of the elliptic problem reads [16]

$$J_E(x, y, x', y', f) = 2\omega - (x'^2 + y'^2) - 2e_p \int_{f_0}^{f} \frac{\Omega \sin \tilde{f}}{(1 + e_p \cos \tilde{f})^2}\, \mathrm{d}\tilde{f} \tag{6}$$

For a given energy level C, Eq. (6) defines the variable manifold [18]

$$\mathcal{J}_E(C, f) = \{(x, y, x', y') \in \mathbb{R}^4 | J_E(x, y, x', y', f) - C = 0\} \tag{7}$$

Setting $e_p = 0$ in Eq. (6) yields the classic Jacobi integral of the circular problem

$$J_C(x, y, \dot{x}, \dot{y}) = 2\Omega - (\dot{x}^2 + \dot{y}^2) \tag{8}$$

together with the associated, steady manifold of the states of motion

$$\mathcal{J}_C(C) = \{(x, y, \dot{x}, \dot{y}) \in \mathbb{R}^4 | J_C(x, y, \dot{x}, \dot{y}) - C = 0\} \tag{9}$$

Once the energy level is specified, manifold (9) defines allowed and forbidden regions of motion, bounded by the Hill's curves. These properties remain fixed in time. As the independent variable f appears in Eq. (6) (both in the function ω and in the integral term on the right-hand side), any qualitative statement on allowed and forbidden regions is no longer possible in the elliptic problem. In particular, *pulsating* Hill's curves appear. These curves vary according to the motion of P_2 about P_1. Reference [19] elaborates on the integral (6) to define subregions of motion under suitable assumptions on variation of the true anomaly.

To better understand the implications of Eq. (6), Fig. 2 reports the Hill's curves associated to the same initial condition, $\boldsymbol{x}_0 = (x_0, y_0, x_0', y_0')$, but different initial anomalies f_0. In Fig. 2a Hill's curves open at L_1, and a passage from the region of P_2 to the neighborhood of P_1 is possible. This is not the case for Fig. 2b where Hill's curves are closed. Thus, as the initial anomaly plays a key role in the motion of P_3, the pair $(\boldsymbol{x}_0, f_0)$ must be specified when referring to a generic initial condition.

C. Regularization

Computing stable sets involves integrating many thousands of orbits, and some of them can turn out to be collisions of P_3 with either P_1 or P_2. In such cases, the numerical integration of Eqs. (1) is singular or ill posed when $r_{1,2} \to 0$. This causes the integrator either to fail or to meet the integration tolerance at the cost of a prohibitive reduction of the integration step-size. It is therefore necessary to regularize the equations of motion (1) to both avoid such singularities and improve the efficiency of the numerical integration. Levi–Civita transformation is convenient to use. It is a local regularization method that maps the physical coordinates (x, y) into the complex plane (u, v) where singularities are removed [17,20]. Two different transformations are used:

$$x + iy = \boldsymbol{w}^2 - \mu \tag{10}$$

in a neighborhood of P_1 and

$$x + iy = \boldsymbol{w}^2 + (1 - \mu) \tag{11}$$

around P_2, with $\boldsymbol{w} = u + iv$, $i = \sqrt{-1}$.

For both transformations, the regularized vector field is deduced from the general expression given in [16]. This yields

$$\begin{aligned} \frac{\mathrm{d}^2 u}{\mathrm{d}\tau^2} - 8\frac{\mathrm{d}v}{\mathrm{d}\tau}(u^2 + v^2) &= \frac{\partial}{\partial u}[4V_i(u^2 + v^2)] - 8uI \\ \frac{\mathrm{d}^2 v}{\mathrm{d}\tau^2} + 8\frac{\mathrm{d}u}{\mathrm{d}\tau}(u^2 + v^2) &= \frac{\partial}{\partial v}[4V_i(u^2 + v^2)] - 8vI \end{aligned} \tag{12}$$

where derivatives are carried out with respect to the new independent variable, τ, which is related with the true anomaly through $\mathrm{d}f/\mathrm{d}\tau = 4(u^2 + v^2)$. Using this relation, the last term in Eq. (12) yields $I = e_p \int_{\tau_0}^{\tau} 4(u^2 + v^2)\Omega \sin f/(1 + e_p \cos f)^2\, \mathrm{d}\tau$. The potential in Eq. (12) is

$$V_1 = \frac{1}{1 + e_p \cos f}\left\{\frac{1}{2}[(u^2 + v^2)^2 - 2\mu(u^2 - v^2) + \mu^2] + \frac{1 - \mu}{r_{1,1}} + \frac{\mu}{r_{2,1}} + \frac{1}{2}\mu(1 - \mu)\right\} - \frac{C}{2} \tag{13}$$

with

$$r_{1,1} = (u^2 + v^2), \qquad r_{2,1} = [(u^2 + v^2)^2 - 2(u^2 - v^2) + 1]^{1/2} \tag{14}$$

for P_1, and

$$V_2 = \frac{1}{1 + e_p \cos f}\left\{\frac{1}{2}[(u^2 + v^2)^2 + 2(1 - \mu)(u^2 - v^2) + (1 - \mu)^2] + \frac{1 - \mu}{r_{1,2}} + \frac{\mu}{r_{2,2}} + \frac{1}{2}\mu(1 - \mu)\right\} - \frac{C}{2} \tag{15}$$

with

$$r_{1,2} = [(u^2 + v^2)^2 + 2(u^2 - v^2) + 1]^{1/2}, \qquad r_{2,2} = (u^2 + v^2) \tag{16}$$

for P_2.

In practice, transformations (10) and (11) are applied when P_3 enters a disc of radius r_{LC_i} centered at P_i, $i = 1, 2$. Inside this disc

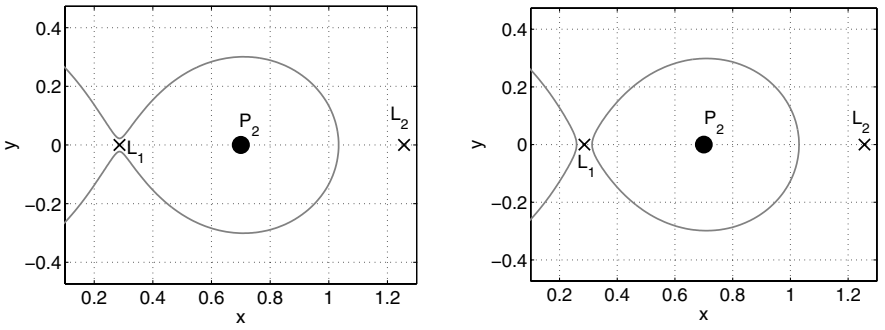

a) $J_E(\boldsymbol{x}_0, f_0) = 3.93,\ f_0 = 0$ b) $J_E(\boldsymbol{x}_0, f_0) = 4.36,\ f_0 = \pi$

Fig. 2 Regions of motion in a neighborhood of P_2 associated to $\boldsymbol{x}_0 = (1, 0, 0.25, 0.3)$, with $\mu = 0.3, e_p = 0.05$. Although the same state is considered and moderate eccentricity is assumed, Hill's curves are opened or closed at L_1, according to the value of the initial anomaly.

Eqs. (12) are integrated. Outside these circles, either standard Eqs. (1) or those in polar coordinates are used. In this paper it has been assumed $r_{\mathrm{LC}_{1,2}} = 10^{-3}$.

D. Polar Coordinates

It is convenient to introduce polar coordinates for our analysis. With reference to Fig. 1, polar coordinates (r_1, θ_1) relative to P_1 define a rotating reference frame with one axis aligned with the P_1P_3 line and the second one perpendicular to it. In this reference frame, P_3 moves under the equations

$$\begin{aligned} r_1'' - r_1\theta_1'^2 - 2r_1\theta_1' &= \frac{1}{1+e_p\cos f}\left[r_1\left(1-\frac{\mu}{r_2^3}\right) - \frac{1-\mu}{r_1^2}\right. \\ &\quad \left. + \mu\cos\theta_1\left(\frac{1}{r_2^3}-1\right)\right] \\ r_1\theta_1'' + 2r_1'\theta_1' + 2r_1' &= \frac{\mu\sin\theta_1}{1+e_p\cos f}\left(1-\frac{1}{r_2^3}\right) \end{aligned} \tag{17}$$

with $r_2 = \sqrt{r_1^2 - 2r_1\cos\theta_1 + 1}$. Similarly, using the coordinates (r_2, θ_2) relative to P_2, the motion of P_3 is governed by

$$\begin{aligned} r_2'' - r_2\theta_2'^2 - 2r_2\theta_2' &= \frac{1}{1+e_p\cos f}\left[r_2\left(1-\frac{1-\mu}{r_1^3}\right) - \frac{\mu}{r_2^2}\right. \\ &\quad \left. + (1-\mu)\cos\theta_2\left(1-\frac{1}{r_1^3}\right)\right] \\ r_2\theta_2'' + 2r_2'\theta_2' + 2r_2' &= \frac{(1-\mu)\sin\theta_2}{1+e_p\cos f}\left(\frac{1}{r_1^3}-1\right) \end{aligned} \tag{18}$$

with $r_1 = \sqrt{r_2^2 + 2r_2\cos\theta_2 + 1}$.

Both systems (17) and (18) are equivalent to Eqs. (1). Polar coordinates are used when either θ_1 or θ_2 are wanted as smooth functions of the independent variable f. However, due to the presence of trigonometric functions, integrating vector fields in polar coordinates is more computationally intensive than treating Cartesian coordinates.

III. Definition of Stable Sets

It is possible to show that in the elliptic problem the Kepler energy of P_3 relative to P_2 reads

$$H_2(f) = \frac{1}{2}v_2^2(f) - \frac{\mu}{r_2(1+e_p\cos f)} \tag{19}$$

where v_2 is the speed of P_3 relative to a P_2-centered inertial reference frame. Using polar coordinates (r_2, θ_2), v_2 can be rearranged as

$$v_2^2(f) = \left(\frac{r_2 e_p\sin f}{1+e_p\cos f} + r_2'\right)^2 + r_2^2(1+\theta_2')^2 \tag{20}$$

Equations (19) and (20) show that H_2 depends on the current value of anomaly f; i.e., for a given state $\boldsymbol{x} = (r_2, \theta_2, r_2', \theta_2')$, the Kepler energy relative to P_2 varies according to the mutual motion of P_1, P_2. This is true even in case the state is constant. This feature is considerably different from the circular problem, and highlights the fundamental role of the independent variable in evaluating the ballistic capture condition.

A. Definition of Stable Sets

Let $\boldsymbol{x}(f)$ be a solution of Eq. (1). P_3 is ballistically captured by P_2 at f_1 if $H_2(\boldsymbol{x}(f_1)) < 0$, and it is temporarily ballistically captured (or weakly captured) by P_2 if $H_2(\boldsymbol{x}(f)) < 0$ for $f_1 \le f \le f_2$ and $H_2(\boldsymbol{x}(f)) > 0$, for $f < f_1$ and $f > f_2$, and for finite anomalies f_1, f_2, $f_1 < f_2$. Regarding the opposite type of behavior, P_3 is ballistically ejected (or ballistically escapes) from P_2 at f_1 if $H_2(\boldsymbol{x}(f)) < 0$ for $f < f_1$ and $H_2(\boldsymbol{x}(f)) \ge 0$ for $f \ge f_1$ (see [1] for a detailed definition of ballistic capture). The region where weak capture occurs can be used to define stable sets. In the following, stable sets are defined using the formalism introduced in [11,12] with proper modifications to adapt to the elliptic restricted three-body problem.

For a fixed value of true anomaly, P_3 is initially set at the periapsis of an osculating prograde ellipse around P_2. In this case

$$r_2(f_0) = a(1-e) \tag{21}$$

where a and e are the semimajor axis and the eccentricity of the osculating ellipse, respectively; f_0 is the value of the initial anomaly. Moreover, trajectories of P_3 satisfying the following conditions are considered.

1) The initial position of P_3 is on a radial segment $l(\theta)$ departing from P_2 and making an angle θ with the P_1P_2 line, relative to the rotating system. The trajectory is assumed to start at the periapsis of an osculating ellipse around P_2, whose semimajor axis lies on $l(\theta)$ and whose eccentricity e is held fixed along $l(\theta)$.

2) In the P_2-centered inertial frame, the initial velocity of the trajectory is perpendicular to $l(\theta)$, and the Kepler energy of P_3 relative to P_2 is negative; i.e., $H_2 < 0$ (ellipse periapsis condition). The motion, for fixed values of e_p, f_0, θ, and e depends on the initial distance r only.

3) The motion is said to be n-stable if the infinitesimal mass P_3 leaves $l(\theta)$, makes n complete revolutions about P_2, $n \ge 1$, and returns to $l(\theta)$ on a point with negative Kepler energy with respect to P_2, *without* making a complete revolution around P_1 along this trajectory. The motion is otherwise said to be n-unstable (Fig. 3).

It is worth observing that the motion of P_3 is unstable if either P_3 performs a full circle about P_2 and returns on $l(\theta)$ on a point where $H_2 \ge 0$ or P_3 moves away from P_2 and performs a full circle about P_1. The former is a ballistic escape, the latter is said primary interchange escape [1].

The set of n-stable points on $l(\theta)$ is a countable union of open intervals

$$\mathcal{W}_n(\theta, e, f_0) = \bigcup_{k\ge 1}(r_{2k-1}^*, r_{2k}^*) \tag{22}$$

with $r_1^* = 0$. The points of type r^* (the endpoints of the intervals above, except for r_1^*) are n-unstable. Thus, for fixed pairs (e, f_0), the collection of n-stable points is

$$\mathcal{W}_n(e, f_0) = \bigcup_{\theta\in[0,2\pi]} \mathcal{W}_n(\theta, e, f_0) \tag{23}$$

The weak stability boundary of order n, denoted by $\partial\mathcal{W}_n$, is the locus of all points $r^*(\theta, e, f_0)$ along the radial segment $l(\theta)$ for which there is a change of stability of the trajectory; i.e., $r^*(\theta, e, f_0)$ is one of the endpoints of an interval (r_{2k-1}^*, r_{2k}^*) characterized by the fact that, for all $r \in (r_{2k-1}^*, r_{2k}^*)$, the motion is n-stable, and there exist $\tilde{r} \notin (r_{2k-1}^*, r_{2k}^*)$, arbitrarily close to either r_{2k-1}^* or r_{2k}^* for which the motion is n-unstable. Thus

$$\partial\mathcal{W}_n(e, f_0) = \{r^*(\theta, e, f_0) | \theta \in [0, 2\pi]\}$$

B. Backward Stability

It is now convenient to define backward ballistic capture. With the same formalism of the previous section, P_3 is *backward* temporary ballistically captured by P_2 if $H_2(\boldsymbol{x}(f)) < 0$ for $f_2 \le f \le f_1$ and if

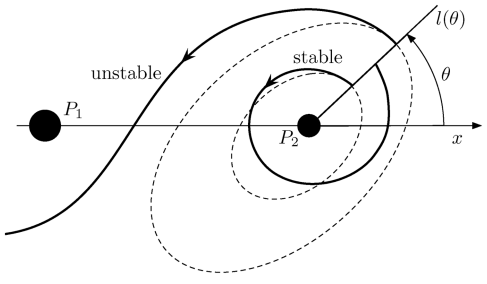

Fig. 3 Example of 1-stable and unstable trajectories relative to P_2.

$H_2(\boldsymbol{x}(f)) > 0$ for $f > f_1$ and $f < f_2$, for finite anomalies f_2, f_1, $f_2 < f_1$. To take into account backward stability, the definition of $-m$-stable orbits is introduced by adding the following condition to the algorithmic definition given above.

4) The motion is said to be $-m$-stable if the orbit of P_3, *backward* integrated, leaves $l(\theta)$, makes m complete turns about P_2, $m \geq 1$, and returns to $l(\theta)$ on a point with negative Kepler energy with respect to P_2, *without* making a complete turn around P_1 along this trajectory. The motion is otherwise said to be $-m$-unstable.

The set of $-m$-stable initial conditions on $l(\theta)$ is a countable union of open intervals

$$\mathcal{W}_{-m}(\theta, e, f_0) = \bigcup_{k\geq 1}(r^*_{2k-1}, r^*_{2k}) \tag{24}$$

where, again, the points of type r^* are backward unstable. For fixed values of osculating eccentricity and initial anomaly, $\mathcal{W}_{-m}$ is defined as

$$\mathcal{W}_{-m}(e, f_0) = \bigcup_{\theta\in[0,2\pi]} \mathcal{W}_{-m}(\theta, e, f_0) \tag{25}$$

and the weak stability boundary of order $-m$ is $\partial\mathcal{W}_{-m}$.

Having extended the definition of stable orbits given in [11,12] to the case of backward integration is of paramount importance to formulate a method that automatically delivers ballistic capture orbits with prescribed stability number. In essence, orbits are sought such that, when integrated forward, they describe a desired number of revolutions about P_2, and, when integrated backward, they ballistically escape from P_2. These two conditions can be achieved in a straightforward manner once n-stable and $-m$-stable sets are constructed. This is explained in Sec. IV.

C. Computation of Stable Sets

Generating stable sets means finding the portion of configuration space (r_2, θ_2) that gives rise to stable orbits for fixed values of e, f_0. In practice, this involves defining a computational grid of initial conditions. This is achieved by setting the periapsis altitudes and polar angles through

$$\begin{aligned} h^i &= h^L + (i-1)\frac{h^U - h^L}{N_h - 1}, \qquad i = 1, \ldots, N_h \\ \theta^j &= \theta^L + (j-1)\frac{\theta^U - \theta^L}{N_\theta - 1}, \qquad j = 1, \ldots, N_\theta \end{aligned} \tag{26}$$

where lower and upper periapsis altitudes, $h^{L,U}$, are suitably chosen based on the pair of primaries selected and their mass parameter; bounds for polar angles are $\theta^L = 0$, $\theta^U = 2\pi$, unless a particular sector is of interest. The total number of initial conditions on the grid is $N_{ic} = N_h N_\theta$.

To fit with practical applications, the altitudes in Eq. (26) are assumed to be in dimensional units (e.g., in km), and, therefore, the corresponding radii for the definition of the initial conditions are given by

$$r^i = (R_{\text{eq}} + h^i)/R_{12}(f_0) \tag{27}$$

where R_{eq} is the mean equatorial radius of P_2, and $R_{12}(f_0)$ is the P_1P_2 distance at the beginning of the integration; i.e., $R_{12}(f_0) = a_p(1 - e_p^2)/(1 + e_p \cos f_0)$ and a_p is the semimajor axis. Each pair (r^i, θ^j) uniquely identifies an initial condition to be flown under the equations of the elliptic restricted three-body problem. Considering Eqs. (17) and (18) in place of Eqs. (1) is a more natural choice to derive the stable sets as the stability condition can be inferred by tracking the angles $\theta_1(t)$ and $\theta_2(t)$. Indeed, P_3 completes a full turn about P_2 at $f = f^*$ if

$$|\theta_2(f^*) - \theta_2(f_0)| = 2\pi \tag{28}$$

for the smallest $f^* > f_0$ such that condition (28) is satisfied. Analogously, P_3 performs a primary interchange escape at $f = f^*$ if

$$|\theta_1(f^*) - \theta_1(f_0)| = 2\pi \tag{29}$$

If condition (28) is verified (and the orbit is such that $H_2(f^*) < 0$) the motion is stable, otherwise, if condition (29) is satisfied, the orbit is unstable. Thus, to assess the stability of the motion, both θ_1 and θ_2 have to be handled as smooth functions of time. This is possible by simultaneously integrating systems (17) and (18) with initial conditions

$$\begin{aligned} r_2(f_0) &= r^i, \qquad \theta_2(f_0) = \theta^j, \qquad r_2'(f_0) = -\frac{r^i e_p \sin f_0}{1 + e_p \cos f_0} \\ \theta_2'(f_0) &= \sqrt{\frac{\mu(1+e)}{(r^i)^3(1 + e_p \cos f_0)}} - 1 \end{aligned} \tag{30}$$

for system (18), and

$$\begin{aligned} r_1(f_0) &= \sqrt{(r^i)^2 + 2r^i \cos\theta^j + 1}, \theta_1(f_0) \\ &= \tan^{-1}\left(\frac{r^i \sin\theta^j}{1 + r^i \cos\theta^j}\right) \\ r_1'(f_0) &= r_2'(f_0)\cos(\theta^j - \theta_1(f_0)) \\ &\quad - r_2(f_0)\theta_2'(f_0)\sin(\theta^j - \theta_1(f_0)) \\ \theta_1'(f_0) &= \frac{r_2'(f_0)}{r_1(f_0)}\sin(\theta^j - \theta_1(f_0)) \\ &\quad + \frac{r_2(f_0)\theta_2'(f_0)}{r_1(f_0)}\cos(\theta^j - \theta_1(f_0)) \end{aligned} \tag{31}$$

for system (17). Integrating Eqs. (17) and (18) in the range $[f_0, f^*]$ is more efficient than flowing Eqs. (1) in a wider range of anomalies. This is shown in [12] for the circular problem. Condition (28) is written in the rotating frame. The number of turns that P_3 performs about P_2 may be different when the trajectory is mapped into the P_2-centered inertial frame.

D. Stable Sets in the Sun–Mars System

Some stable sets about Mars are computed. The physical parameters used in these computations are reported in Table 1. To represent the stable sets with appropriate resolution, and to limit at the same time the computational burden, initial periapsis altitudes are defined on a nonuniform grid. The grid is finer in the region close to P_2 and coarser in the rest of the space; that is:

$$\begin{aligned} h^i &= h^L + (i_1 - 1)\frac{h^{U_1} - h^L}{N_{h_1} - 1} + (i_2 - 1)\frac{h^{U_2} - h^{U_1}}{N_{h_2} - 1} \\ i_1 &= 1, \ldots, N_{h_1}; i_2 = 1, \qquad i_2 = 1, \ldots, N_{h_2}; i_1 = N_{h_1} \end{aligned} \tag{32}$$

with $h^L = 250$ km, $h^{U_1} = 30050$ km, $h^{U_2} = 250000$ km, $N_{h_1} = 597$, $N_{h_2} = 440$. The set of angles θ_2 is defined by the second of Eq. (26), with $\theta^L = 0$, $\theta^U = 2\pi$, $N_\theta = 362$. The total number of initial conditions is therefore $N_{ic} = N_\theta(N_{h_1} + N_{h_2}) = 375394$.

The dependence of the stable sets geometry on the mass ratio has been discussed in [12]. The variation of stable sets with the initial anomaly f_0 is shown here. Figure 4 reports $\mathcal{W}_1(f_0, e)$ sets for $f_0 = \{0, 0.5\pi, \pi\}$, $e = 0.95$. It is convenient remarking that the grid of initial conditions (r^i, θ^j), and in particular the distances r^i, vary with the initial true anomaly f_0 in the elliptic problem. This happens because the dimensional altitudes h^i are kept fixed, whereas the initial dimensionless distances are given by Eq. (27). Figure 4d shows the set of -1-stable initial conditions, $W_{-1}(\pi, 0.95)$. This set

Table 1 Problem parameters, sun–Mars case (a_p in AU; R_{eq} in km)

μ	e_p	a_p	$r_{\text{LC}_{1,2}}$	R_{eq}
$3.226208 \cdot 10^{-7}$	0.093418	1.523688	10^{-3}	3397

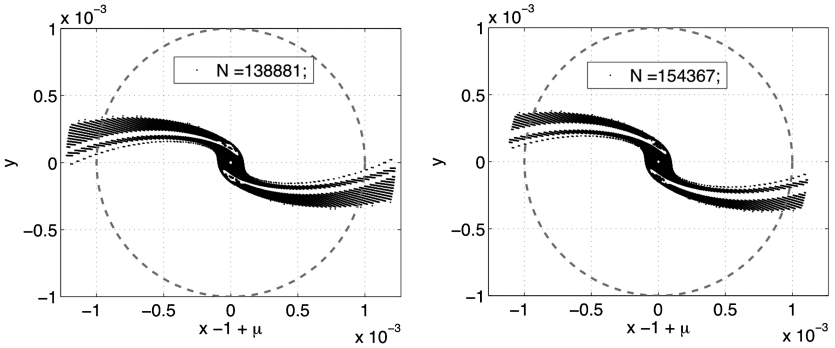

a) $W_1(0, 0.95)$ b) $W_1(0.5\pi, 0.95)$

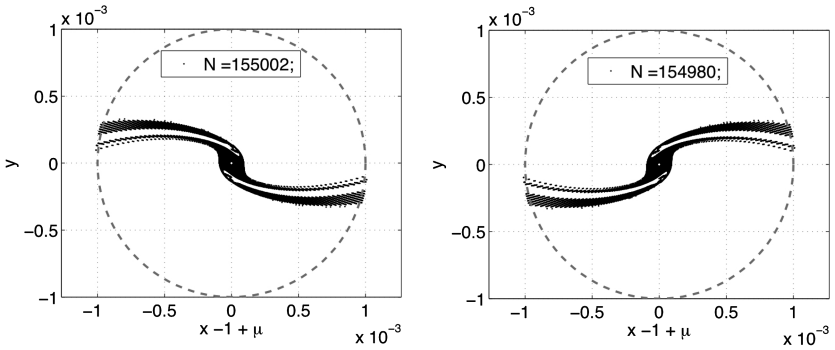

c) $W_1(\pi, 0.95)$ d) $W_{-1}(\pi, 0.95)$

Fig. 4 1-stable sets in the sun–Mars case for different values of f_0 and $e = 0.95$. The stable sets tend to shrink for increasing initial true anomaly. N is the number of stable initial conditions. The dashed circle encloses the Levi–Civita regularizing disc. The -1-stable set is reported bottom-right for $f_0 = \pi$, $e = 0.95$.

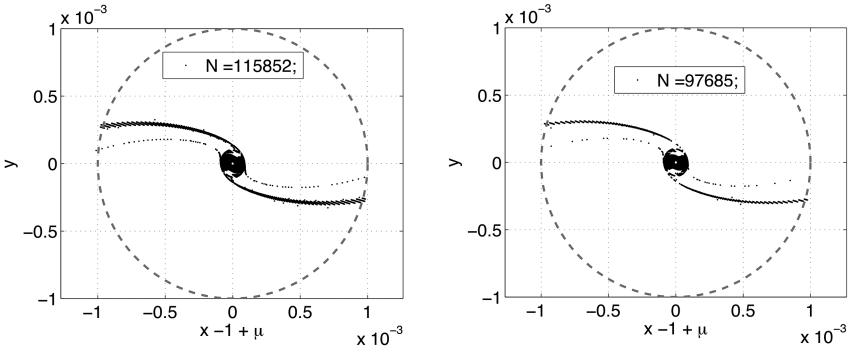

a) $W_2(\pi, 0.95)$ b) $W_3(\pi, 0.95)$

Fig. 5 2-stable and 3-stable sets in the sun–Mars case; $f_0 = \pi$, $e = 0.95$. N is the number of stable initial conditions.

will be used in the following, together with sets $\mathcal{W}_2(\pi, 0.95)$ and $\mathcal{W}_3(\pi, 0.95)$ reported in Fig. 5.

IV. Construction of Ballistic Capture Orbits with Prescribed Stability Number

Given two stability numbers, $(l, h) \in \mathbb{Z}\backslash\{0\}$, and given the pair (e, f_0), the stable sets $W_l(e, f_0)$, $W_h(e, f_0)$ can be computed using the technique illustrated above. These sets contain l-stable and h-stable initial conditions, respectively. Note that the positiveness of the two stability numbers is not required. The *intersection* between two sets is defined as

$$\mathcal{W}_l^h(e, f_0) = \mathcal{W}_l(e, f_0) \cap \mathcal{W}_h(e, f_0) = \{(r^i, \theta^j) \in \mathcal{W}_l(e, f_0), (r^i, \theta^j) \in \mathcal{W}_h(e, f_0)\} \tag{33}$$

The set $\mathcal{W}_l^h(e, f_0)$ contains initial conditions that are *both* l-stable and h-stable. If $h \geq l$, then $\mathcal{W}_h \subseteq \mathcal{W}_l$. As the initial radii depend on f_0, the two sets have to be defined at the same value of f_0 to identify common positions r^i. Moreover, the two sets must be computed for the same osculating eccentricity e to achieve the same initial velocity.

Let us now consider the case $l = -1$, $h = n \geq 1$. In this case, the set $\mathcal{W}_{-1}^n$ contains orbits that are both -1-stable and n-stable. Initial conditions $(r^i, \theta^j) \in \mathcal{W}_{-1}^n(e, f_0)$ perform at least n revolutions about P_2 if integrated forward, and at least 1 revolution about P_2 if integrated backward. Thus, P_3 performs at least $n + 1$ revolutions about P_2, and therefore the set $\mathcal{W}_{-1}^n$ is equivalent to $\mathcal{W}_{n+1}$.

Given a stable set, $\mathcal{W}_l(e, f_0)$, its *complementary* is defined as

$$\bar{\mathcal{W}}_l(e, f_0) = \{(r^i, \theta^j) \notin \mathcal{W}_l(e, f_0)\} \tag{34}$$

i.e., $\bar{\mathcal{W}}_l$ is made up by initial conditions that are *not* l-stable. In principles, (r^i, θ^j) may be defined over the entire physical space, but only the l-unstable initial conditions defined over the computational grid (26) are considered. In case $l = -1$, the set $\bar{\mathcal{W}}_{-1}$ is made up by initial conditions that are -1-unstable: these points yield orbits that escape from P_2 when integrated backward.

To derive practical orbits with prescribed stability number the *capture* set is defined as

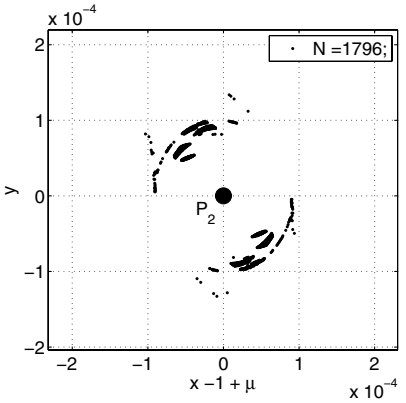

Fig. 6 Capture set $\mathcal{C}^3_{-1}(\pi, 0.95)$, sun–Mars case. N is the number of stable initial conditions.

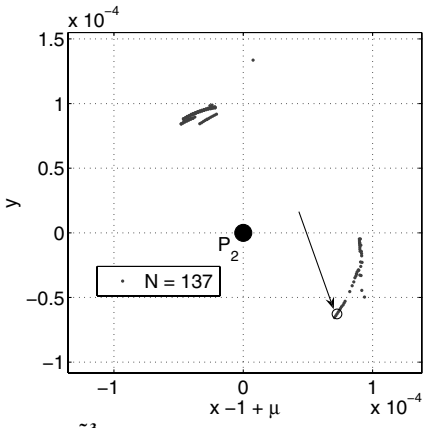

Fig. 7 Capture set $\tilde{\mathcal{C}}^3_{-1}(\pi, 0.95)$ after the application of the filters, sun–Mars case. N is the number of filtered, stable initial conditions.

$$\mathcal{C}^{\,n}_{-1}(e, f_0) = \bar{\mathcal{W}}_{-1}(e, f_0) \cap \mathcal{W}_n(e, f_0) \tag{35}$$

The initial conditions contained in $\mathcal{C}^n_{-1}$ have the following properties:

1) They are -1-unstable; i.e., these initial conditions escape from P_2 when integrated backward. This means that these orbits approach P_2 in forward time.

2) They are n-stable; i.e., these initial conditions generate orbits that perform at least n revolutions about P_2.

Thus, if the backward and forward pieces are patched together, the orbits in $\mathcal{C}^n_{-1}$ approach P_2 (either from P_1 or the exterior region) and stay about it for at least n turns. This is desirable for missions analysis, as orbits contained in $\mathcal{C}^n_{-1}$ are good candidate orbits to design ballistic capture upon arrival at P_2.

Figure 6 shows the set $\mathcal{C}^3_{-1}(\pi, 0.95)$ computed in the sun–Mars case. This set is achieved by intersecting $\mathcal{W}_{-1}(\pi, 0.95)$ in Fig. 4d and $\mathcal{W}_3(\pi, 0.95)$ in Fig. 5b. Again, initial conditions in Fig. 6 generate orbits that approach Mars and perform at least three revolutions about it.

Ballistic Escape: Ballistic escape has been defined in Sec. III. Like ballistic capture, ballistic escape may be used in space trajectory design to reduce the propellant mass necessary to leave a planet [21]. Using the same formalism above, a set containing ballistic escape trajectories may be defined as

$$\mathcal{E}^{\,1}_{-m} = \{\mathcal{W}_{-m}(e, f_0) \cap \bar{\mathcal{W}}_1(e, f_0)\} \tag{36}$$

The set $\mathcal{E}^1_{-m}$ contains orbits that are $-m$-stable ($m \geq 1$) and 1-unstable; i.e., the orbits perform m revolutions about P_2 before escaping from it. This definition relies, once again, on the stable sets, and ballistic escape orbits may be found once the stable sets have been computed.

V. Application to Interplanetary Transfers

The set $\mathcal{C}^n_{-1}$ is obtained by intersecting the complement of the -1-stable set, $\bar{\mathcal{W}}_{-1}$, with $\mathcal{W}_n$. The former contains -1-unstable conditions; i.e., initial conditions that generate orbits either not completing a full turn about P_2 or returning on $l(\theta)$ with positive Kepler energy when integrated backward (see the algorithmic definition in Sec. III). Unstable orbits returning on $l(\theta)$ are not useful for practical applications. Thus, only a subset of $\mathcal{C}^n_{-1}$ has to be considered to design ballistic capture. To do this, $\mathcal{C}^n_{-1}$ is filtered to select only those solutions of practical interest. Two kinds of filters are applied.

1) Energetic filter: This step selects only those initial conditions whose orbits have nonnegative Kepler energy when integrated backward after the first ballistic escape condition. This means that orbits having Kepler energy that oscillates about zero are pruned away. Strictly speaking, only initial conditions producing backward temporary ballistic escape are preserved (Sec. III.B).

2) Geometric filter: This filter keeps track of the direction along which P_3 leaves the P_2 region backward in time. Only orbits approaching P_2 from the proper direction are considered. This means that, for instance, if a ballistic capture from P_1 region is desired, orbits approaching P_2 from the exterior region have to be discarded and vice versa.

The energetic filter is general, and it is used to find backward escape trajectories. The geometric filter depends on the transfer at hand. In the sun–Mars case discussed so far, to design Earth–Mars transfer with ballistic capture, the capture is constrained to occur from the inner side, Earth's orbit being inside that of Mars. Thus, the initial conditions that bring P_3 outside the orbit of Mars backward in time are discarded.

The filtered set is denoted by $\tilde{\mathcal{C}}$. Figure 7 shows the capture set $\tilde{\mathcal{C}}^3_{-1}$ (in Fig. 6) after the application of the filters. Being N the number of points in both figures, it can be seen that less than 10% of the initial conditions obtained through $\bar{\mathcal{W}}_{-1} \cap \mathcal{W}_n$ survive after the application of the filters. Nevertheless, these initial conditions are well clustered into two different regions, showing robustness with respect to small variations of the target point selected. Moreover, points in Fig. 7 may support the interplanetary trajectory design as they represent first guess solutions to be refined in a more realistic scenario, taking into account fourth-body and nongravitational perturbations.

A. Transfers to Mars with Ballistic Capture

The filtered set shown in Fig. 7 is used to design ballistic captures at Mars. As each point of $\tilde{\mathcal{C}}^3_{-1}(\pi, 0.95)$ is a feasible solution, the point indicated by the arrow is analyzed. For the sake of evaluating the complete Earth–Mars transfer, the arrival capture portion is linked to a low-thrust trajectory departing from the Earth. The latter, defined in the two-body problem, is designed using a shape-based approach [15]. Thus, the endpoint of the low-thrust leg is patched to the beginning of the ballistic capture. Although the two pieces are defined into two different models (two-body problem for the low-thrust trajectory and elliptic restricted three-body problem for the capture orbit), this approach has shown to be valid at least in the preliminary trajectory design framework [8]. An analytical ephemeris model has also been used to describe planets' motion.

Figure 8 illustrates the solution found. The whole interplanetary trajectory, made up by low-thrust arc and ballistic capture portion, is shown in Fig. 8a. In Fig. 8b the ballistic capture at Mars is shown in the Mars-centered frame where the dashed line is the orbit in $\bar{\mathcal{W}}_{-1}$ ($f < f_0$) and the solid line is in $\mathcal{W}_3$ ($f > f_0$). It can be seen that the trajectory flown about Mars is strongly non-Keplerian, therefore it cannot be found using classical tools such as the patched-conics method. Figure 8c shows the capture orbit in the sun–Mars rotating frame. To show the usefulness of having studied the elliptic problem over the *circular* one, the ballistic capture condition has been integrated into these two models. The orbit in the elliptic problem (solid) considerably differs from that obtained in the circular problem (dashed), with the latter leading to impact with Mars. This indicates that the ballistic capture studied in this work, which lasts hundreds of days, is better described when the planet's eccentricity is considered,

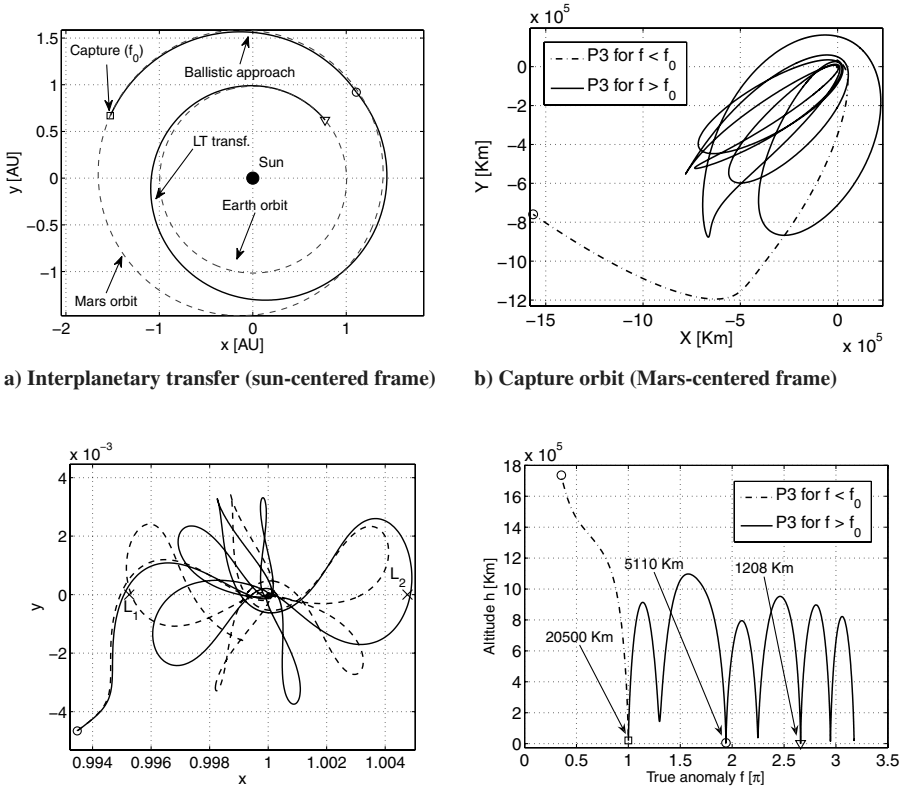

a) Interplanetary transfer (sun-centered frame) **b) Capture orbit (Mars-centered frame)**

c) Capture orbit (rotating frame). Elliptic problem (solid); circular problem (dashed) **d) Altitude profile during capture**

Fig. 8 Low-thrust, ballistic capture transfer to Mars.

although this introduces a more complicated dynamics. Figure 8d shows the altitude profile during capture. Although the solid line is defined in $\mathcal{W}_3$, it can be seen that more than three chances exist to stabilize the spacecraft in a final, low-Mars orbit, if required. This occurs as the condition on the number of revolutions about P_2 (Eq. (28)) is imposed in the rotating frame. Moreover, in this specific case, P_3 reverses the direction of the angular momentum in orbiting P_2; thus, it performs further close encounters with Mars.

Even if designing low-thrust interplanetary transfers is beyond the scope of this paper, basic features characterizing the transfer in Fig. 8 are given. The times-of-flight are 485, 240, and approximately 750 days for the low-thrust leg, the approaching portion, and the orbit about Mars, respectively. The propellant mass fraction is 0.164 considering both no hyperbolic velocity at departure from Earth and a specific impulse of 3000 s. The maximum acceleration is $2.3 \cdot 10^{-4}$ m/s^2. This is easily achievable with current low-thrust engines and typical spacecraft masses.

B. Ballistic Capture at Mercury

The method described in this paper is used to define ballistic capture solutions at Mercury. This option is the baseline solution for BepiColombo mission, where a ballistic capture is being preferred to a classic hyperbolic approach to avoid single-point failures of chemical, high-thrust engines. The interplanetary trajectory is not considered in this case as it is obtained by optimizing low-thrust, multiple gravity assist orbits, which are both not trivial to achieve and beyond the scope of this paper [4].

The computational grid considered is the one described in Eqs. (26) with $h^L = 50$ km, $h^U = 5000$ km, $\theta^L = 0$, $\theta^U = 2\pi$, $N_h = 331$, and $N_\theta = 722$. The total number of initial conditions is therefore $N_{ic} = 238982$. The chosen parameters are $f_0 = 0$ and $e = 0.96$. The radii of the regularizing discs are $r_{\mathrm{LC}_{1,2}} = 10^{-3}$.

Some stable sets are shown in Fig. 9, together with a sample capture solution at Mercury. In particular, the set of six-stable initial conditions, $\mathcal{W}_6(0, 0.96)$, has been computed to match the constraint of orbiting Mercury 6 times at least. As the eccentricity of Mercury is nonnegligible, the stable sets have been computed in both the elliptic and circular problems to assess once again the properness of the former in describing long-term captures. Figures 9a and 9b illustrate $\mathcal{W}_1$ and $\mathcal{W}_6$, respectively, in the elliptic (black) and circular (gray) problems. These sets differ in size and shape, with the sets obtained in the elliptic problem showing wider stable areas, leading to a higher number of feasible solutions. In general it can be seen that the six-stable condition considerably reduces the number of feasible points. For what concerns the elliptic problem, the set $\tilde{\mathcal{C}}^6_{-1}(0, 0.96)$ is shown in Fig. 9c. This set is filtered by applying both the energetic and geometric conditions. Note that approaches from the exterior are desired here. Therefore orbits escaping Mercury toward the inner region are pruned away. The sample solution indicated in Fig. 9c is analyzed in the subsequent pictures. In Fig. 9d the ballistic capture condition is integrated both in the elliptic (solid) and circular (dashed) problems, and presented in the sun–Mercury rotating frame. The orbits show different features, so confirming once again the usefulness of having studied the elliptic restricted three-body problem to analyze long-term capture. In Fig. 9e the orbit in the elliptic problem is shown in the Mercury-centered inertial frame, whereas its altitude profile is reported in Fig. 9f. Again, as the condition on the number of turns is imposed in the rotating frame, there are more than six close encounters with Mercury where possible stabilization maneuvers can be carried out.

C. Discussion

Although the method is constructed to find ballistic capture orbits by using the set $\mathcal{C}^n_{-m}$, i.e., orbits that are $-m$-unstable and n-stable, solutions of the kind $\mathcal{C}^n_{-1}$ have been looked for. The choice $m = 1$ is driven by the fact that trajectories immediately escaping P_2 (without orbiting it) have been searched. All subsequent stable revolutions are considered into $\mathcal{W}^n$. Thus, solutions of the kind $\mathcal{C}^n_{-m}$ may also exist. In principles, it is also possible to use this method for matching orbits about the two primaries of the restricted problem; i.e., to construct

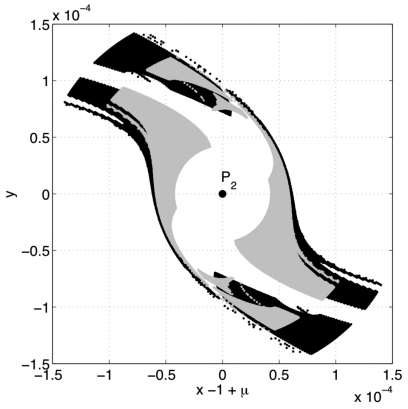

a) $W_1(0, 0.96)$. Elliptic problem (black); circular problem (gray)

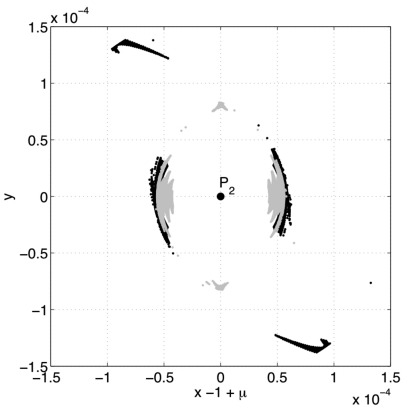

b) $W_6(0, 0.96)$. Elliptic problem (black); circular problem (gray)

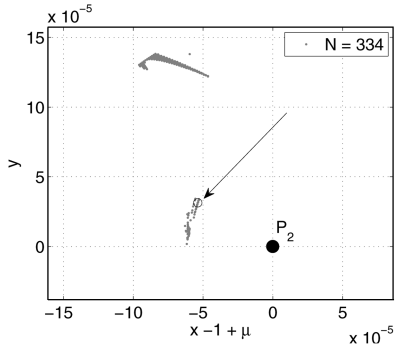

c) $\tilde{C}^6_{-1}$ (0, 0.96), filtered

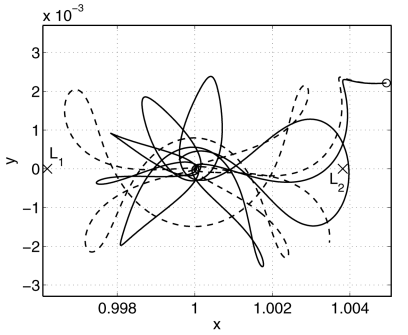

d) Capture orbit (rotating frame). Elliptic problem (solid); circular problem (dashed)

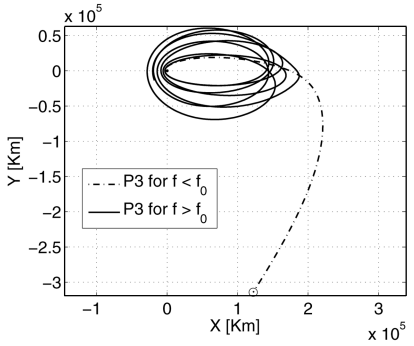

e) Capture orbit (Mercury-centered frame)

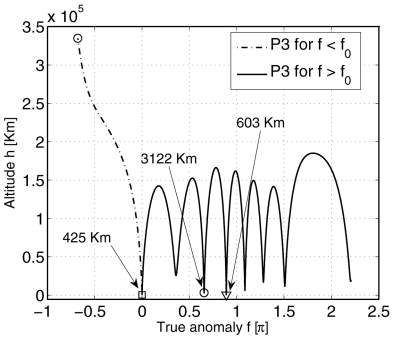

f) Altitude profile during capture

Fig. 9 Stable sets, capture set, and a sample capture orbit at Mercury.

orbits from P_1 to P_2 it is enough joining unstable orbits about P_1 with stable orbits about P_2. This may be useful, for instance, to construct Earth–moon transfers with ballistic capture at the moon.

The role played by the planetary eccentricity in the capture dynamics is clearly shown by Figs. 8c and 9d. Ignoring such eccentricity and integrating the capture condition under the circular problem produces orbits which are significantly different from those obtained in the elliptic problem. There is also evidence that the stable sets obtained in the elliptic problem are larger than those defined in the circular problem (see Figs. 9a and 9b). Moreover, it has been found that the number of stable points reduces for increasing orbital eccentricity of the planets, so decreasing the chances of capture as discussed in [9].

In general, the method delivers solutions that perform a higher number of prescribed revolutions about the planet when viewed in the planet-centered frame. This is an appealing feature as it gives more chances to stabilize the spacecraft with a single-impulse maneuver, though it would be desirable to have more control on the number of loops. Moreover, only sets obtained for a fixed value of f_0 can be intersected. The question of finding the best f_0 to design the capture remains open. Valuable insights can be gained by studying the dynamics of zero-velocity curves with respect to variations of true anomaly [19]. Alternatively, the value of f_0 can be restricted within a small range once the arrival epoch at the planet is given with some tolerance. Finally, the osculating eccentricity associated to the initial conditions is assumed fixed by mission constraints. This is realistic although having some rationales on how to choose the best value of e would be desirable.

VI. Conclusions

In this paper, a method to design ballistic capture orbits about the smaller primary in the elliptic restricted three-body problem has been formulated. This method automatically delivers orbits with a prescribed stability number, provided that the corresponding stable sets are computed. The method relies on a relatively simple algorithmic definition that keeps track of both the number of revolutions and the Kepler energy of the massless particle about the smaller

primary. Thus, the algorithm can be easily extended to more refined dynamical frameworks (e.g., full ephemeris models) in a straightforward way. This is not so trivial for invariant manifolds technique.

The algorithm is also based on general principles: it can be applied in the neighborhood of the smaller primary of any restricted three-body problem. It has been here applied to find ballistic capture orbits about both Mars and Mercury, in the sun-Mars and sun-Mercury problems, respectively. These models have been selected as the circular problem fails in describing the three-body dynamics due to the nonnegligible planetary eccentricities of Mars and Mercury. It has been demonstrated that ignoring such eccentricity, i.e., studying the circular problem, may result in incorrect ballistic capture orbits.

The paper elaborates on previous works dealing with stable sets, weak stability boundaries, and their computations. These works are useful to understand the capture dynamics of the third body in the regions about the primaries. The present paper describes instead how to *use* this information to design a ballistic capture orbit for mission analysis purposes.

Acknowledgments

The authors are grateful to Steven Kemble for having provided useful data on BepiColombo mission analysis. The authors would like to thank anonymous reviewers for their valuable comments. Francesco Topputo is grateful to both Pierluigi Di Lizia and Sharlene Hay for useful feedback given.

References

[1] Belbruno, E., *Capture Dynamics and Chaotic Motions in Celestial Mechanics: With Applications to the Construction of Low Energy Transfers*, Princeton Univ. Press, Princeton, NJ, 2004, pp. 111–114, 145–150.

[2] Belbruno, E., and Miller, J., "Sun-Perturbed Earth-to-Moon Transfers with Ballistic Capture," *Journal of Guidance, Control, and Dynamics*, Vol. 16, No. 4, 1993, pp. 770–775. doi:10.2514/3.21079

[3] Schoenmaekers, J., Horas, D., and Pulido, J. A., "SMART-1: With Solar Electric Propulsion to the Moon," *Proceeding of the 16th International Symposium on Space Flight Dynamics*, Pasadena, CA, 2001.

[4] Jehn, R., Campagnola, S., García, D., and Kemble, S., "Low-Thrust Approach and Gravitational Capture at Mercury," *Proceedings of the 18th International Symposium on Space Flights Dynamics*, Vol. 584, ESA, Noordwick, The Netherlands, 2004, p. 487.

[5] Koon, W., Lo, M., Marsden, J., and Ross, S., "Heteroclinic Connections between Periodic Orbits and Resonance Transitions in Celestial Mechanics," *Chaos*, Vol. 10, No. 2, 2000, pp. 427–469. doi:10.1063/1.166509

[6] Gómez, G., Koon, W., Lo, M., Marsden, J., Masdemont, J., and Ross, S., "Invariant Manifolds, the Spatial Three-Body Problem and Space Mission Design," *Advances in the Astronautical Sciences*, Vol. 109, No. 1, 2001, pp. 3–22.

[7] Koon, W., Lo, M., Marsden, J., and Ross, S., "Low Energy Transfer to the Moon," *Celestial Mechanics and Dynamical Astronomy*, Vol. 81, Nos. 1–2, 2001, pp. 63–73. doi:10.1023/A:1013359120468

[8] Topputo, F., Vasile, M., and Bernelli-Zazzera, F., "Low Energy Interplanetary Transfers Exploiting Invariant Manifolds of the Restricted Three-Body Problem," *Journal of the Astronautical Sciences*, Vol. 53, 2005, pp. 353–372.

[9] Astakhov, S., and Farrelly, D., "Capture and Escape in the Elliptic Restricted Three-Body Problem," *Monthly Notices of the Royal Astronomical Society*, Vol. 354, No. 4, 2004, pp. 971–979. doi:10.1111/j.1365-2966.2004.08280.x

[10] Gawlik, E., Marsden, J., Du Toit, P., and Campagnola, S., "Lagrangian Coherent Structures in the Planar Elliptic Restricted Three-Body Problem," *Celestial Mechanics and Dynamical Astronomy*, Vol. 103, No. 3, 2009, pp. 227–249. doi:10.1007/s10569-008-9180-3

[11] García, F., and Gómez, G., "A note onWeak Stability Boundaries," *Celestial Mechanics and Dynamical Astronomy*, Vol. 97, No. 2, 2007, pp. 87–100. doi:10.1007/s10569-006-9053-6

[12] Topputo, F., and Belbruno, E., "Computation of Weak Stability Boundaries: Sun-Jupiter System," *Celestial Mechanics and Dynamical Astronomy*, Vol. 105, Nos. 1–3, Nov. 2009, pp. 3–17. doi:10.1007/s10569-009-9222-5

[13] Romagnoli, D., and Circi, C., "Earth–Moon Weak Stability Boundaries in the Restricted Three and Four Body Problem," *Celestial Mechanics and Dynamical Astronomy*, Vol. 103, No. 1, 2009, pp. 79–103. doi:10.1007/s10569-008-9169-y

[14] Belbruno, E., Gidea, M., and Topputo, F., "Weak Stability Boundary and Invariant Manifolds," *SIAM Journal on Applied Dynamical Systems*, Vol. 9, No. 3, pp. 1061–1089.

[15] Wall, B., and Conway, B., "Shape-Based Approach to Low-Thrust Rendezvous Trajectory Design," *Journal of Guidance, Control, and Dynamics*, Vol. 32, No. 1, Jan.–Feb. 2009, pp. 95–101. doi:10.2514/1.36848

[16] Szebehely, V., *Theory of Orbits: The Restricted Problem of Three Bodies*, Academic Press Inc., New York, 1967, pp. 587–602.

[17] Kechichian, J., "Local Regularization of the Restricted elliptic Three-Body Problem in Rotating Coordinates," *Journal of Guidance, Control, and Dynamics*, Vol. 25, No. 6, Nov.–Dec. 2002, pp. 1064–1072. doi:10.2514/2.5011

[18] Dvorak, R., "The Jacobian Constant in the Elliptic, Restricted Three-Body Problem," *Astronomische Gesellschaft and Deutsche Forschungsgemeinschaft*, Vol. 42, March 1977, pp. 75–77.

[19] Campagnola, S., Lo, M., and Newton, P., "Subregions of Motion and Elliptic Halo Orbits in the Elliptic Restricted Three-Body Problem," *Proceedings of the 18th AIAA/AAS Space Flight Mechanics Meeting*, AAS Paper 08-200, 2008.

[20] Celletti, A., *Chaotic Worlds: From Order to Disorder in Gravitational N-Body Dynamical Systems*, Springer–Verlag, New York, 2006, Chap. Basics of Regularization Theory, pp. 203–230.

[21] Topputo, F., Belbruno, E., and Gidea, M., "Resonant Motion, Ballistic Escape, and their Applications in Astrodynamics," *Advances in Space Research*, Vol. 42, No. 8, Oct. 2008, pp. 6–17.